

1 **Efficient Two-Terminal All-Perovskite Tandem Solar Cells Enabled**
2 **by High-Quality Low-Bandgap Absorber Layers**

3 Dewei Zhao,^{1*,#} Cong Chen,^{1,2#} Changlei Wang,^{1,2#} Maxwell M. Junda,¹ Zhaoning Song,¹
4 Corey R. Grice,¹ Yue Yu,¹ Chongwen Li,¹ Biwas Subedi,¹ Nikolas J. Podraza,¹ Xingzhong
5 Zhao,² Guojia Fang,² Ren-Gen Xiong,^{3,4} Kai Zhu,⁵ Yanfa Yan^{1*}

6 ¹Department of Physics and Astronomy and Wright Center for Photovoltaics Innovation and
7 Commercialization, The University of Toledo, Toledo, Ohio 43606, United States

8 ²Key Laboratory of Artificial Micro/Nano Structures of Ministry of Education, School of
9 Physics and Technology, Wuhan University, Wuhan 430072, China

10 ³Ordered Matter Science Research Center, Nanchang University, Nanchang 330031, P. R.
11 China

12 ⁴Jiangsu Key Laboratory for Science and Applications of Molecular Ferroelectrics, Southeast
13 University, Nanjing 211189, P. R. China.

14 ⁵Chemistry and Nanoscience Center, National Renewable Energy Laboratory, Golden,
15 Colorado 80401, United States

16
17 ***Corresponding Authors**

18 D.W.Z: dewei_zhao@hotmail.com; Y.F.Y: yanfa.yan@utoledo.edu

19 **Author Contributions**

20 # D.Z., C.C., and C.L.W. contributed equally to this work.

21

22

1 **Abstract**

2 **Multi-junction all-perovskite tandem solar cells are a promising choice for next-**
3 **generation solar cells with high efficiency and low fabrication cost. However, the lack of**
4 **high-quality low-bandgap perovskite absorber layers seriously hampers the development**
5 **of efficient and stable two-terminal monolithic all-perovskite tandem solar cells. Here, we**
6 **report a bulk-passivation strategy via incorporation of chlorine, to enlarge grains and**
7 **reduce electronic disorder in mixed tin-lead low-bandgap (~1.25 eV) perovskite absorber**
8 **layers. This enables the fabrication of efficient low-bandgap perovskite solar cells using**
9 **thick absorber layers (~750 nm), which is a requisite for efficient tandem solar cells. Such**
10 **improvement enables the fabrication of two-terminal all-perovskite tandem solar cells**
11 **with a champion power conversion efficiency of 21% and steady-state efficiency of 20.7%.**
12 **The efficiency is retained to 85% of its initial performance after 80 hours of operation**
13 **under continuous illumination.**

14

1 Organic-inorganic lead halide perovskite solar cells (PVSCs) have attracted tremendous
2 interest due to the rapid increase in record power conversion efficiency (PCE) of single-junction
3 devices from 3.8% to a certified 23.3%¹⁻⁴. Low-temperature solution processability and
4 bandgap tunability make the metal halide perovskites an ideal candidate for fabricating all-
5 perovskite tandem solar cells, which can overcome the Shockley-Queisser (SQ) radiative
6 efficiency limits for single-junction cells. For two-terminal (2-T) monolithic tandem devices
7 consisting of a wide-bandgap (wide- E_g) top subcell (~ 1.7 - 1.9 eV)⁵ and a low-bandgap (low- E_g)
8 bottom subcell (~ 1.1 - 1.3 eV)^{6,7}, the predicted maximum PCE is over 40%^{8,9}.

9 Thus far, efficient 2-T tandem cells based on perovskite/Si, perovskite/copper indium
10 gallium diselenide (Cu(In,Ga)Se₂), and perovskite/perovskite configurations have been
11 reported^{8,10-13}. Among them, the all-perovskite tandem cells possess unique advantages,
12 including low-temperature processes for all subcells, compatibility with flexible and
13 lightweight applications, and potentially low fabrication costs^{9,14,15}. Recently, McGehee, Snaith,
14 and co-workers reported a 2-T all-perovskite tandem cell with a PCE of 17%⁸. Bolink and co-
15 workers combined solution-processed wide- E_g perovskite top cells with vacuum-deposited
16 medium-bandgap (~ 1.5 - 1.6 eV) perovskite bottom cells to build 2-T tandem cells with a
17 champion PCE of 18.1%¹². Jen and co-workers achieved a PCE of 18.5% for a 2-T all-
18 perovskite tandem cell using a 1.82 eV wide- E_g top cell and a 1.22 eV low- E_g bottom cell¹³.

19 For a 2-T tandem cell, current matching between the two subcells plays a crucial role in
20 the final performance of the device. The electronic quality of the low- E_g perovskite absorber
21 layer is particularly important since it requires a thick layer to fully absorb the infrared light
22 passing through the wide- E_g subcell¹⁶. A thick absorber layer without high electronic quality
23 would inevitably result in a solar cell with a relatively low fill factor (FF) and open-circuit
24 voltage (V_{oc}) due to the non-radiative recombination losses occurring in the bulk perovskite layer
25 and at the perovskite/charge-selective layer interfaces¹⁷⁻²¹. Many efforts have been made to
26 reduce the non-radiative recombination losses in various-bandgap PVSCs via passivating the

1 surface and bulk^{21,22}, enlarging grains^{16,23,24}, and engineering the contacts/heterojunction
2 interface²⁵. Unlike in their wide and medium bandgap perovskite counterparts, efficiency
3 improvement in low- E_g PVSCs is rarely reported due to the difficulty and challenge to process
4 high-quality low- E_g perovskite absorber layers. However, such improvement is essential for
5 fabricating efficient 2-T all-perovskite tandem cells.

6 Here, we report on the increase in grain size and reduction of electronic disorder in low- E_g
7 mixed Sn-Pb perovskite layers via incorporating chlorine (Cl). Such improvements allow us to
8 successfully fabricate efficient 1.25 eV low- E_g PVSCs with thick absorber layers (~750 nm)
9 without sacrificing either FF or V_{oc} . By combining these low- E_g perovskite bottom subcells
10 with 1.75 wide- E_g perovskite top subcells and ultra-flat and compact interconnecting layers
11 (ICLs), we fabricate 2-T all-perovskite tandem cells with PCEs approaching 21%. An
12 encapsulated tandem solar cell with an efficiency greater than 20% retains 85% of its initial
13 performance after 80 hours of continuous operation under 1 sun illumination in air as measured
14 by maximum power point tracking.

15

16 **Photovoltaic performance of low- E_g PVSCs with Cl incorporation**

17 We incorporated Cl into mixed tin (Sn)-lead (Pb) low- E_g perovskite^{16,26} by mixing
18 stoichiometric molar ratio of $(\text{FASnI}_3)_{0.6}(\text{MAPbI}_y\text{Cl}_{3-y})_{0.4}$ ($0 < y < 3$) and $(\text{FASnI}_3)_{0.6}(\text{MAPbI}_3)_{0.4}$
19 to form a $(\text{FASnI}_3)_{0.6}(\text{MAPbI}_{3-3x}\text{Cl}_{3x})_{0.4}$ precursor ($x = 0, 1.25\%, 2.5\%, 5\%, \text{ and } 10\%$) (FA =
20 formamidinium, MA = methylammonium, I = iodide) (**see the Methods**), leading to a
21 consistent molar ratio of Sn to Pb at 0.6:0.4. Although E_g shows a monotonic minor increase as
22 a function of Cl concentration (**Supplementary Fig. 1a and 1b, and Supplementary Methods**),
23 the overall change in E_g is less than 0.8%, suggesting that the effect of Cl incorporation on E_g
24 is practically irrelevant, i.e., these perovskites retain their bandgap values at ~1.25 eV. X-ray
25 diffraction (XRD) patterns of $(\text{FASnI}_3)_{0.6}(\text{MAPbI}_3)_{0.4}$ films with varying Cl concentrations
26 reveal no differences (**Supplementary Fig. 2**), implying that the change in Cl concentration

1 does not influence crystal structure and grain orientation of (FASnI₃)_{0.6}(MAPbI₃)_{0.4} films. All
2 XRD patterns show a highly preferred orientation of the (110) planes of the orthorhombic
3 perovskite phase^{16,26}. Scanning electron microscopy (SEM) images reveal the increase in grain
4 size with the increase of Cl concentration (**Supplementary Fig. 3**), similar to the effect of Cl
5 seen in pure Pb perovskites^{27,28}. We find that the larger grains and/or higher crystallinity in our
6 mixed Sn-Pb perovskite films, originating from Cl facilitated grain growth, are remarkably
7 beneficial for device performance.

8 We fabricate inverted planar PVSCs with a structure reported in our previous works^{16,26,29}:
9 indium-doped tin oxide (ITO)/poly(3,4-ethylenedioxythiophene):polystyrene sulfonate
10 (PEDOT:PSS)/(FASnI₃)_{0.6}(MAPbI₃)_{0.4} /fullerene (C₆₀)/2,9-dimethyl-4,7-diphenyl-1,10-
11 phenanthroline (BCP)/Ag. We vary the Cl concentration in the perovskite layers and achieve
12 the best performance at the incorporation of 2.5% Cl (**Supplementary Fig. 4 and**
13 **Supplementary Table 1**). Henceforth, we chose two sets of PVSCs with 0.0% Cl as a control
14 (referred as to Sn/Pb-0.0%Cl) and 2.5% Cl for comparison (referred as to Sn/Pb-2.5%Cl), to
15 investigate the effects of Cl incorporation on the perovskite film quality and solar cell
16 performance.

17 **Figure 1a** shows the current density-voltage (*J-V*) curves of our best-performing Sn/Pb-
18 0.0%Cl and Sn/Pb-2.5%Cl PVSCs. The Sn/Pb-2.5%Cl cell shows a PCE of 18.40 (18.40)%
19 with a V_{oc} of 0.850 (0.842) V, a short-circuit current density (J_{sc}) of 29.31 (29.40) mA cm⁻², and
20 a fill factor (FF) of 73.9 (74.4)%, however, the Sn/Pb-0.0%Cl control cell shows a PCE of 17.29
21 (17.09)% with a V_{oc} of 0.822 (0.824) V, a J_{sc} of 29.29 (29.22) mA cm⁻², and a fill factor (FF) of
22 71.8 (71.0)%, when measured under forward (reverse) voltage scan. Both cells exhibit a
23 negligible degree of *J-V* hysteresis. To the best of our knowledge, the champion PCE of 18.4%
24 is so far the highest efficiency for low- E_g PVSCs (~1.1-1.3 eV) reported in the literature.
25 Importantly, our cells use 750 nm thick absorber layers, ensuring high external quantum
26 efficiency (EQE) values in the 700 to 900 nm IR wavelength range (**Fig. 1b**), which is desirable

1 and beneficial for a successful tandem cell performance. The integrated J_{sc} 's over the AM 1.5G
2 solar spectrum for Sn/Pb-0.0%Cl and Sn/Pb-2.5%Cl cells are 28.59 and 28.69 mA cm⁻²,
3 respectively, in good agreement with the J_{sc} 's extracted from the J - V characterizations. We have
4 fabricated 50 Sn/Pb-2.5%Cl devices in several batches. The PCE histogram (**Fig. 1c**) implies
5 that our cells have very good reproducibility. The increase in average V_{oc} (from 0.815 to 0.834
6 V) and average FF (from 70.9% to 73.5%) (**Supplementary Fig. 5 and Supplementary**
7 **Table 2**) clearly shows the performance benefits of incorporating a small amount of Cl in the
8 precursor solution.

9

10 **Characterization of low- E_g perovskites with Cl incorporation**

11 To gain further insight into the efficiency improvement due to the incorporation of Cl, we
12 characterize perovskite film properties/quality, charge carrier mobility, and charge
13 recombination in solar cells without Cl and with 2.5% Cl. As shown in **Fig. 2a and 2b**, after
14 the incorporation of 2.5% Cl, the grain size becomes comparable with the film thickness (~750
15 nm thick). The full width at half maximum (FWHM) values of the (110) peak from XRD
16 patterns of Sn/Pb-0.0%Cl and Sn/Pb-2.5%Cl are 0.099° and 0.087°, respectively
17 (**Supplementary Fig. 6**), indicating an increase in crystallinity upon the incorporation of Cl.
18 The near-unity aspect ratio of the grains implies a low number of horizontal grain boundaries
19 (i.e., oriented perpendicular to the net charge transport direction) which could cause excessive
20 carrier scattering and recombination. Thereby, the resulting grain morphology from the
21 incorporation of Cl likely facilitates efficient charge transport inside the device, leading to
22 improved V_{oc} and FF. Moreover, it has been demonstrated that the Cl ions segregate onto and
23 passivate grain boundaries in MAPbI₃ perovskite films to enhance device performance^{30,31}. A
24 similar passivation effect is also expected in mixed Sn-Pb perovskite films.

25 We further conduct the photothermal deflection spectroscopy (PDS) measurements to
26 assess the effect of Cl incorporation on the semiconductor quality and electronic disorder in the

1 mixed Sn-Pb perovskite films. The PDS technique detects below bandgap absorption with a
2 high dynamic range of sensitivity (4-5 orders of magnitude), in which a steeper slope of the
3 absorption indicates a lower electronic disorder in a semiconductor³²⁻³⁴. We then derive the
4 Urbach energy (E_u) as an indicator of electronic disorder using $A(E) \propto e^{E/E_u}$, where A is the
5 absorbance and E is the excitation energy in electron volts, as shown in **Fig. 2c** and
6 **Supplementary Methods**. Upon the incorporation of 2.5% Cl, the E_u decreases from $27.9 \pm$
7 1.1 to 23.9 ± 0.75 meV, corresponding to a decrease in the density of trap states^{35,36}, which is
8 consistent with the enhanced crystallinity suggested by the decreased FWHM value of XRD
9 peaks and with the increase in grain size shown by the SEM images. We emphasize that the
10 absorption spectra of Sn/Pb-0.0%Cl and Sn/Pb-2.5%Cl perovskite films determined by PDS
11 measurements show almost identical bandgaps (**Fig. 2c and inset**).

12 The enhanced crystallinity and lower trap density induced by the Cl incorporation should
13 result in reduced charge carrier scattering at grain boundaries and ionized defects, leading to
14 higher charge carrier mobility. We perform transient photocurrent measurements using a
15 modified method following a recent report³⁷ to assess the effect of the Cl incorporation on carrier
16 transport in the devices. We use a 532 nm laser light with 10 and 50 μ s pulses to excite transient
17 photocurrents in the active area of the device, i.e., the overlap area of two electrodes, and on
18 the Ag electrode at a distance, L , of 1 to 5 mm away from the current quench edge of the ITO
19 electrode that is outside of the active area, respectively (**Supplementary Fig. 7a and 7b**).
20 Illumination on the active area aims to probe the transport behavior of minority carriers
21 (electrons). Because of the high absorption coefficient of the Sn-Pb perovskite, charge carriers
22 are preferentially generated near to the front contact of the device. Photoexcited holes can
23 rapidly inject into the hole selective contact (ITO/PEDOT:PSS), leaving the electrons to diffuse
24 through the perovskite layer and be collected at the electron selective contact (C₆₀/BCP/Ag).
25 The decay behavior of the transient photocurrent is mainly determined by the trapping and

1 recombination rates of minority carriers. We observed longer photocurrent decay time (292 μs)
2 in the Sn/Pb-2.5%Cl cell than that (172 μs) in the Sn/Pb-0.0%Cl cell (**Fig. 2d**), indicating
3 increased minority carrier mobility and lifetime after the incorporation of Cl. To investigate the
4 majority carrier transport behavior, we moved the photoexcitation to the Ag area outside the
5 active area (**Supplementary Fig. 7c**). This transient photocurrent is dominant by the hole
6 diffusion in the perovskite layer because photoexcited electrons are rapidly collected by the Ag
7 electrode (paired with the electron selective layer) at the location under illumination while holes
8 need to diffuse > 1 mm to the ITO electrode to be collected. The variations in transient current
9 amplitude and arrival time as a function of L are shown in **Fig. 2e and 2f**. With increasing
10 distance, the photocurrent amplitude decreased and the arrival time increased by almost one
11 order of magnitude. By using numerical simulations of charge diffusion dynamics to fit the
12 transient photocurrent data (see **Methods section** and **Supplementary Methods**), we are able
13 to estimate hole mobility in the perovskite absorber. The mobilities, $\mu = 40 \pm 5 \text{ cm}^2 \text{ V}^{-1} \text{ s}^{-1}$ for
14 Sn/Pb-2.5%Cl film and $\mu = 27 \pm 2 \text{ cm}^2 \text{ V}^{-1} \text{ s}^{-1}$ for Sn/Pb-0.0%Cl film, indicate that the inclusion
15 of Cl decrease the density of defects and increase the diffusion lengths of charge carriers, which
16 is consistent with the measured trend of E_u and crystallinity. Importantly, the collection of
17 photocurrent excited outside the active area of device (**Supplementary Fig. 8**), as evidenced
18 by laser beam induced current (LBIC) mapping technique³⁸, indicates that J_{sc} of low- E_g PVSCs
19 can be significantly overestimated if an aperture is not used in the J - V measurements. Such J_{sc}
20 overestimation is observed in organic solar cells when the devices are overfilled by the
21 illumination source³⁹.

22 To further examine the charge extraction and charge recombination processes in these solar
23 cells, we perform light-intensity-dependence J - V measurements on Sn/Pb-0.0%Cl and Sn/Pb-
24 2.5%Cl low- E_g PVSCs. **Fig. 2g** shows the power law dependence of the J_{sc} on light intensity
25 ($J \propto I^\alpha$). The α values of 0.97 and 0.98 for Sn/Pb-0.0%Cl and Sn/Pb-2.5%Cl cells, respectively,

1 are both close to unity, suggesting no significant energy barrier and space charge limited
2 current during the charge extraction process²⁴. The V_{oc} as a function of light intensity is plotted
3 in **Fig. 2h** for Sn/Pb-0.0%Cl and Sn/Pb-2.5%Cl cells. V_{oc} appears to increase monotonically
4 with logarithmic light intensity, indicating that trap-assisted Shockley–Read–Hall
5 recombination is dominant in these devices. The ideality factor n of 1.27 for the Sn/Pb-2.5%Cl
6 cell is smaller than that of 1.65 for the Sn/Pb-0.0%Cl cell, consistent with the reduction in
7 electronic disorder in Cl-incorporated low- E_g perovskite film³⁴.

8

9 **2-Terminal All-perovskite Tandem Solar Cells**

10 We fabricate 2-T all-perovskite tandem cells with 1.75 eV perovskite top cells (~250 nm)
11 and 2.5% Cl-incorporated 1.25 eV perovskite bottom cells (~720 nm), as illustrated in **Fig. 3a**
12 **and 3b**. For 2-T all-perovskite monolithic tandem cells, the interconnecting layer (ICL)
13 provides optical and electrical connection as well as full protection of the underlying layers
14 during fabrication of the subsequent bottom subcells. Although several ICLs in 2-T all-
15 perovskite tandem cells have been employed such as SnO₂/ITO⁸, TaTm:F6TCNNQ/C₆₀:PhIm¹²,
16 and Bis-C₆₀/ITO⁴⁰ (**Supplementary Table 3**), it is still highly desired to explore a facile ICL
17 combination obtainable through easily accessible and processable component materials. We use
18 vacuum-processed multiple stack of ultra-thin Ag (1 nm), MoO_x (3 nm), and ITO (~120 nm) as
19 the ICL. Ag and MoO_x layers were thermally evaporated, and ITO was deposited by sputtering.
20 The MoO_x layer prevents damage to the BCP/Ag layers caused by the sputtering of ITO and
21 ensures good contact between Ag and ITO. These multiple layers smoothen the 1.75 eV
22 perovskite layer (**Supplementary Fig. 9**) and enable an extremely flat and smooth ICL without
23 any pinholes (**Fig. 3b and Supplementary Fig. 10**), which well protects the underlying 1.75
24 eV perovskite subcell from solvent damage^{8,40}, especially when processing water-containing
25 PEDOT:PSS. This robust ICL allows us to fabricate the 1.25 eV Sn/Pb-2.5%Cl subcell ontop.
26 Additionally, our ICL possesses transmittance of over 70% in the wavelength range from 720

1 to nearly 900 nm, allowing good light harvesting by the low- E_g perovskite bottom subcell
2 (**Supplementary Fig. 11**).

3 When measured under the reverse (forward) voltage scans, the champion 2-T tandem cell
4 achieves a PCE of 21.0 (20.6)%, which is higher than the single perovskite top cell, 14.0
5 (13.7)%, and the single perovskite bottom cell, 18.1 (18.1)% (**Fig. 3c, inset of Fig. 3c,**
6 **Supplementary Fig. 12, and Table 1**). The corresponding steady-state efficiency is 20.7%
7 (**Fig. 3d**). In the 2-T tandem cell, the ultra-thin Ag layer acts as recombination center⁴¹. In
8 comparison, a 2-T tandem cell without the 1 nm Ag layer exhibits a significant kink in the J - V
9 curve near the open circuit point (**Supplementary Fig. 13**), indicating charge accumulation at
10 the interface of BCP and MoO_x due to non-Ohmic contact between the two layers. It has been
11 proven in the literature that the insertion of the Ag layer can significantly improve the contact
12 properties^{41,42}. This suggests that electrons from the top subcell and holes from the bottom
13 subcell recombine at the Ag layer effectively, delivering an almost summated V_{oc} of 1.922 V,
14 compared to those of the single top cell (1.15V) and single Sn/Pb-2.5%Cl bottom cell (~0.850
15 V). It is worth mentioning that the bottom subcell in the 2-T tandem cell should produce a
16 slightly lower V_{oc} than the individual 1.25 eV low- E_g cell due to reduction of incident light
17 reaching the bottom subcell¹⁶. The ICL without MoO_x produces a lower V_{oc} and FF
18 (**Supplementary Fig. 13**), likely attributed to formation of a silver oxide layer during sputtering
19 of ITO, which leads to the voltage loss across the ICL.

20 Photocurrent from both subcells must be matched to deliver optimum performance in 2-T
21 tandem cells. Our EQE spectra (**Fig. 3e**) reflect that the photocurrent of 13.7 mA cm⁻² from the
22 top subcell and that of 14.0 mA cm⁻² from the bottom subcell are fairly matched, leading to a
23 reasonable J_{sc} of ~14.0 mA cm⁻² for the 2-T tandem cell. The FF (~78%) of 2-T tandem cell is
24 remarkably high among the values reported in literature^{8,12,40} (**Supplementary Table 3**) and is
25 higher than those of our single top/bottom cells. On one hand, the incorporation of Cl in 1.25
26 eV low- E_g bottom cell improves FFs for the single subcell as previously discussed. On the other

1 hand, the fact that the FF is not limited to the lowest values of the individual subcells results
2 from the tandem configuration^{8,43}. The PCE histogram in **Fig. 3f** suggests good reproducibility
3 of our 2-T all-perovskite tandem cells with an average efficiency of $20.1 \pm 0.4\%$.

4 The PCE of our 2-T all-perovskite tandem cells is mainly limited by the large V_{oc} loss in
5 the wide-bandgap subcell and low J_{sc} of the tandem cell. The former is mostly attributed to the
6 potential halide segregation in wide-bandgap perovskite absorber. Further V_{oc} enhancement is
7 anticipated using alkaline metal (i.e., K^+) doping to suppress the halide phase segregation⁴⁴.
8 The low J_{sc} is mostly caused by the optical losses from the substrate and the ICL. For example,
9 PEDOT:PSS and 120 nm thick ITO can cause parasite absorptions in the long wavelength light.
10 J_{sc} improvement is also anticipated if anti-reflection coating and optimization of ICL are applied.

11 Currently, few studies have reported on the stability of 2-T all-perovskite tandem cells. To
12 evaluate the operational stability of our 2-T tandem cells, we examine the V_{oc} and efficiency as
13 a function of time. The V_{oc} was measured under a continuous 1 sun illumination for over 200 s
14 and the V_{oc} value remained steady at ~ 1.92 V. (**Fig. 3g**). A 2-T tandem solar cell with an
15 efficiency higher than 20% retained 85% of its initial performance after 80 hours of operation
16 under continuous 100 mW cm^{-2} AM 1.5G illumination in air as measured by maximum power
17 point tracking (**Fig. 3h**). Furthermore, an encapsulated cell retained 94% of its initial efficiency
18 after storing in ambient air for 45 days (**Supplementary Fig. 14**). Though such stabilities are
19 not comparable with that of single-junction medium-bandgap perovskite solar cells⁴⁵, these
20 results are encouraging for further improvements of the long-term stability of 2-T all-perovskite
21 tandem solar cells. While the degradation mechanism is expected to be complex, we speculate
22 that the degradation could be attributed to one or the combination of the following possibilities
23 such as light-induced halide phase separation in the wide- E_g perovskite⁵, oxidation of mixed
24 Sn-Pb low- E_g perovskite⁴⁶, imperfections in the UV epoxy sealing⁴⁷, interface degradation
25 induced by ion diffusion (e.g., Ag)^{48,49} and high acidity (e.g., PEDOT:PSS)⁵⁰. Identifying the
26 origins of degradation is subjected to future study.

1

2 **Conclusion**

3 Overall, we found that incorporation of 2.5% Cl enlarges grains, increases crystallinity and
4 carrier mobility, reduces electronic disorder, and suppresses trap-assisted recombination in 1.25
5 eV low- E_g perovskite films, leading to improved performance of devices using thick absorber
6 layers. Combining the optimised bottom subcells with 1.75 eV wide- E_g top subcell and effective
7 ICLs, we successfully fabricated 2-T all-perovskite tandem cell with efficiencies up to ~21%
8 and promising operational stability. Because of the low-temperature solution processing of
9 absorber layers and full vacuum processing of ICLs, our approach is suitable for the fabrication
10 of high-efficiency 2-T all-perovskite tandem cells on flexible plastic substrates thus offering
11 opportunities for cost reduction.

1 **Methods**

2 **Materials and solvents.** Methylammonium iodide (MAI) and formamidinium iodide (FAI)
3 were purchased from GreatCell Solar Company (Australia). Lead bromide (99.999%) was
4 purchase from Tokyo Chemical Industry Co., Ltd. (TCI, Japan). Lead iodide (PbI₂, 99.9985%),
5 cesium iodide (CsI, 99.9%), and diethyl ether were purchased from Alfa Aesar. Tin iodide
6 (SnI₂), N,N-dimethylmethanamide (DMF) (anhydrous), lead thiocyanate (Pb(SCN)₂) (99.5%),
7 PbCl₂, dimethyl sulfoxide (DMSO) (anhydrous), and chlorobenzene (CB) were purchased from
8 Aldrich Sigma. Poly(3,4-ethylenedioxythiophene):polystyrene sulfonate (PEDOT:PSS,
9 CLEVIOS™ P VP AI 4083) was purchased from Heraeus, LLC. Poly [bis (4-phenyl)(2,4,6-
10 trimethylphenyl)amine] (PTAA) were purchased from Xi'an Polymer Light Technology Corp
11 (China). 2,3,5,6-Tetrafluoro-7,7,8,8-tetracyanoquinodimethane (F₄-TCNQ) and bathocuproine
12 (BCP) were purchased from Jilin OLED Company (China). Indium tin oxide (ITO, In₂O₃/SnO₂
13 90/10 wt %) target and silver (Ag) were purchased from Kurt J. Lesker Company. All chemicals
14 used in this work were commercially available and were used as received.

15
16 **1.75 eV FA_{0.8}Cs_{0.2}Pb(I_{0.7}Br_{0.3})₃ wide-E_g perovskite precursor.** the precursor preparation has
17 been reported in our previous works^{51,52}. The precursor solution was prepared by dissolving
18 0.736 mmol FAI, 0.184 mmol CsI, 0.506 mmol PbI₂ and 0.414 mmol PbBr₂ in 1 mL mixed
19 solvents of DMF and DMSO with a volume ratio of 3:1. The precursor solution was thoroughly
20 mixed and aged for 12 hours before use.

21
22 **1.25 eV (FASnI₃)_{0.6}(MAPbI₃)_{0.4} low-E_g perovskite precursor.** the precursor preparation has
23 been reported in our previous works^{16,26}. The FASnI₃ precursor solution was prepared by
24 dissolving 372 mg of SnI₂ and 172 mg of FAI with 10mol % (15.6 mg) of SnF₂ in mixed DMF
25 and DMSO. The MAPbI₃ precursor solution was prepared by dissolving 461 mg PbI₂ and 159
26 mg MAI with 3.5 mol % (11.3 mg) Pb(SCN)₂ dissolved in 630 μL DMF and 70 μL DMSO.

1 The $(\text{FASnI}_3)_{0.6}(\text{MAPbI}_3)_{0.4}$ precursor solution was obtained by mixing stoichiometric amounts
2 of FASnI_3 and MAPbI_3 perovskite precursor. The mixed solutions are kept for 30 min before
3 spin coating.

4
5 **1.25 eV low- E_g perovskite precursor with various Cl concentration.** $\text{MAPbI}_x\text{Cl}_{3-x}$ solution
6 was prepared by dissolving 477 mg MAI and 278 mg PbCl_2 in 850 μL mixed solution of DMF
7 and DMSO ($v:v = 9:1$). FASnI_3 solution was the same as above. The $(\text{FASnI}_3)_{0.6}(\text{MAPbI}_x\text{Cl}_{3-x})_{0.4}$
8 solution was obtained by using stoichiometric molar ratio of corresponding precursors. For
9 1.25 eV low- E_g perovskite precursor with different Cl concentration,
10 the $(\text{FASnI}_3)_{0.6}(\text{MAPbI}_x\text{Cl}_{3-x})_{0.4}$ and $(\text{FASnI}_3)_{0.6}(\text{MAPbI}_3)_{0.4}$ solutions were mixed with various
11 ratios, then the mixed precursors were blended evenly before using.

12
13 **Hole selective layer. Doped-PTAA:** $\text{F}_4\text{-TCNQ}$ in CB with a solution concentration of 1 mg ml^{-1}
14 ¹ was stirred at 60 °C for overnight. Then, $\text{F}_4\text{-TCNQ}$ solution was added into PTAA solution
15 with a concentration of 8 mg ml^{-1} in CB, leading to a weight ratio of 1%. Hole-selective layer:
16 The pre-patterned ITO substrates were cleaned by sequential ultrasonication in diluted Micro-
17 90 detergent, deionized water, acetone, and isopropanol for 15 min, respectively, and then
18 blown-dry with nitrogen gas. For 1.75 eV wide- E_g cells, the ITO substrates were treated by UV-
19 Ozone for 20 min and transferred to a N_2 -filled glovebox with H_2O and O_2 concentrations of
20 <0.1 ppm. $\text{F}_4\text{-TCNQ}$ -doped PTAA layer was obtained by spin-coating the mixed solution onto
21 the ITO substrates at 4000 rpm for 30 s, and then the films were annealed at 120 °C for 15 min.
22 To enhance the wettability of $\text{FA}_{0.8}\text{Cs}_{0.2}\text{Pb}(\text{I}_{0.7}\text{Br}_{0.3})_3$ precursor solution on the PTAA, the
23 ITO/PTAA were pre-treated by 70 μl of DMF, followed by spin-coating at 6000 rpm for 10 s
24 prior to perovskite layer deposition. For 1.25 eV low- E_g single cells, PEDOT:PSS films were
25 coated on the ITO substrates at 4000 rpm for 50 s and then dried at 175 °C for 30 min. Then
26 they were transferred into a glove box filled with N_2 with H_2O and O_2 concentrations of <0.1

1 ppm. For 2-T tandem cells, PEDOT:PSS films were coated on sputtered ITO coated underneath
2 top subcells at 4000 rpm for 50 s and then dried at 110 °C for 5 min. Then they were transferred
3 into the glove box.

4
5 **1.75 eV FA_{0.8}Cs_{0.2}Pb(I_{0.7}Br_{0.3})₃ wide-E_g perovskite film.** The FA_{0.8}Cs_{0.2}Pb(I_{0.7}Br_{0.3})₃ wide-E_g
6 perovskite precursor solution was spin-coated onto the PTAA-coated ITO substrates at 5000
7 rpm for 60 s with 750 μL diethyl ether dripped at 25 s during the spinning. The as-deposited
8 film was annealed at 65 °C for 2 min and then 100 °C for 10 min in an inert atmosphere (N₂).

9
10 **1.25 eV low-E_g perovskite film.** For single cells, the (FASnI₃)_{0.6}(MAPbI₃)_{0.4} precursors with
11 varying Cl concentration (0.0%, 1.25%, 2.5%, 5.0%, and 10.0%) were spin-coated onto
12 ITO/PEDOT:PSS at 5,000 rpm for 60 s. Diethyl ether was applied drop-wise at 5 s onto the
13 spinning substrate during the spin-coating. All perovskite films were annealed at 100 °C for 7
14 min in a glove box. For 2-T tandem cells, the (FASnI₃)_{0.6}(MAPbI₃)_{0.4} precursor with 2.5% Cl
15 was spin-coated onto PEDOT:PSS coated underneath top subcells. Diethyl ether was applied
16 as antisolvent. All perovskite films were annealed at 100 °C for 7 min. The samples for SEM
17 measurement were obtained by spin-coating their corresponding precursor solutions onto
18 ITO/PEDOT:PSS. The samples for UV-Vis spectroscopy were prepared by spin-coating their
19 corresponding precursor solutions onto glass/PEDOT:PSS. The samples for PDS, SE,
20 unpolarized transmittance measurements were coated on glass.

21
22 **Electron selective, interconnecting and electrode layers.** For all cells including single top,
23 single bottom, and 2-T tandem cells, C₆₀(20 nm)/BCP(5 nm)/Ag(75 nm) were sequentially
24 deposited by thermal evaporation in a vacuum chamber at 3×10⁻⁷ torr to complete the entire cell
25 fabrication⁵³. The metal electrode was completed through a metal shadow mask with an
26 overlapped area with pre-patterned ITO of 0.12 cm². For 2-T tandem cells, C₆₀(20 nm)/BCP(5

1 nm)/Ag(1 nm)/MoO_x(3 nm) were sequentially deposited by thermal evaporation in the vacuum
2 chamber without breaking vacuum. Then, the samples were transferred to the sputtering system.
3 About 120 nm ITO layer with a sheet resistance of around 30 Ω/sq was sputtered from a 3"
4 target (Lesker, In₂O₃/SnO₂ 90/10 wt %) at a 100 W power during the second stage under Ar
5 pressure of 1.5 mTorr. The sheet resistance of the ITO layer deposited on glass was measured
6 using a four-point probe method (PRO4-440N, Lucas labs). Right after the deposition of ITO
7 layer, PEDOT:PSS films were spin-coated onto the prepared underneath subcells and post-
8 annealed at 110 °C for 5 min. Devices were encapsulated with cover glass and UV-curable
9 epoxy.

10

11 **SEM.** High resolution field emission top-view SEM images of (FASnI₃)_{0.6}(MAPbI₃)_{0.4}
12 perovskite films with varying Cl concentration and cross-sectional SEM images of the entire 2-
13 T all-perovskite tandem cell were taken with Hitachi S-4800. The perovskite films for SEM
14 measurement were prepared on PEDOT:PSS-coated ITO substrates.

15

16 **AFM.** Surface roughness and topography images were obtained using a Veeco Nanoscope
17 Scanning Probe Microscope to perform atomic force microscopy measurements using a 1-Ohm
18 silicon probe in the tapping mode.

19

20 **Transmittance.** The transmittance spectra were measured by UV-Vis spectrophotometer
21 (PerkinElmer Lambda 1050). All layer thicknesses were determined using a Dektak surface
22 profiler and cross-sectional SEM images. The perovskite films for transmittance measurement
23 were prepared on ITO/PTAA substrates. Then, C₆₀/BCP/Ag/MoO_x/ITO multiple layers were
24 thermally deposited on top of ITO/PTAA/1.75 eV wide-E_g film. The light is incident from the
25 glass side for this measurement.

26

1 **XRD.** The crystal structure of $(\text{FASnI}_3)_{0.6}(\text{MAPbI}_3)_{0.4}$ films with varying Cl concentration was
2 examined by X-ray diffraction (XRD) (RigakuUltima III) with Cu K_α radiation under operation
3 conditions of 40 kV and 44 mA excitation. The perovskite films for XRD measurement were
4 prepared on PEDOT:PSS-coated ITO substrates.

5
6 **Photothermal deflection spectroscopy (PDS) measurement.** The PDS measurements are
7 collected using a custom system (PTS-3-PTD, Sciencetech Inc.) operating in transverse
8 configuration⁵⁴ over a spectral range of 1400 – 800 nm (0.89 – 1.55 eV) in 10 nm steps. The
9 monochromatic pump beam is modulated with a mechanical chopper at 0.2 Hz. The probe beam
10 is a 633 nm laser of nominally 300 μm cross sectional diameter. The full acquisition time for
11 measurement of each film was approximately 5 hours. During PDS measurement, each film is
12 immersed in a quartz cuvette containing a C_6F_{14} fluid (Fluorinert FC-72, Synquest Laboratories)
13 which, in addition to being a thermally sensitive medium suitable for PDS measurement, also
14 effectively eliminates atmospheric exposure of the perovskite films during measurement. For
15 comparison, pristine films of 0, 1.25, 2.5, 5, and 10% Cl were prepared and subsequently
16 immersed in C_6F_{14} with the transfer taking place in a pure N_2 environment. Thus, PDS
17 measurements are collected for perovskite films without exposure to atmosphere.

18
19 **Spectroscopic ellipsometry (SE) and unpolarized transmittance measurement.**
20 Immediately following PDS measurement, each film was removed from the C_6F_{14} fluid into the
21 laboratory ambient for SE and unpolarized transmittance measurements. Both of these
22 measurements were collected using a multichannel rotating-compensator spectroscopic
23 ellipsometer^{55,56} (M-2000FI, J. A. Woollam Co., Inc.) over a spectral range of 1676 – 210 nm
24 (0.74 – 5.89 eV). The SE and unpolarized transmittance measurements were collected at 70°
25 and 0° angle of incidence, respectively, with the SE being measured in terms of $N = \cos(2\psi)$, C
26 $= \sin(2\psi)\cos\Delta$, and $S = \sin(2\psi)\sin\Delta$. The combined time for sample mounting, alignment, and

1 data acquisition for these two measurements, i.e. the length of time the films were in atmosphere,
2 was approximately 5 mins.

3

4 **Transient photocurrent and laser-beam induced current (LBIC) measurement.** A
5 modified LBIC system built in house was used to measure transient photocurrent. The
6 measurements were performed using a light beam generated by a 532 nm Nd:YAG laser
7 operating in the Q-switching mode at a repetition rate of 200 kHz. The beam had a measured
8 Gaussian output width of $\sim 40 \mu\text{m}$ and an average power of $\sim 1 \text{ mW}$ (corresponding to a power
9 density of $\approx 80 \text{ W cm}^{-2}$ or a photon flux of $2.13 \times 10^{20} \text{ photons s}^{-1} \text{ cm}^{-2}$). Laser pulses with a
10 pulse duration of 10 to 50 μs and a delay of 3.5 ms were focused on the device surface at the
11 location controlled by computer programmed overhead galvanometers. The measurement
12 cabinet was covered by absorptive black cloth to minimize light scattering. The time-resolved
13 photocurrent signals were amplified by a current preamplifier (Oriental model 70170) with a gain
14 of 10^6 V A^{-1} and a time constant of 150 μs and recorded by a fast-speed digital oscilloscope
15 (Keysight, model DSOX6002A) operating at a 1 GHz acquisition rate. All temporal
16 photocurrent spectra were averaged over 32 pulses. Finally, the steady-state dark current was
17 subtracted to show the photocurrent response. LBIC measurements were performed by
18 scanning the laser beam across solar cells at a speed of 1 mm s^{-1} with a $30 \mu\text{m}$ spacing between
19 two lateral scans. The photocurrent signals were collected by a Keithley 2601 source meter
20 operating at an acquisition rate of 5 kHz and used to construct a photocurrent map.

21

22 **Solar cell characterizations.** $J-V$ curves were measured in air under 100 mW/cm^2 AM1.5G
23 solar irradiation (PV Measurements Inc.) with a Keithley 2400 Source Meter. The incident light
24 was controlled by a shutter. The exposure of the cells to the light source is short, which does
25 not increase the temperature of the cells. The light intensity for $J-V$ measurements was
26 calibrated by a standard silicon wafer solar cell and our perovskite solar cells certified by

1 Newport. Light intensity dependence measurements were made by decreasing the solar
2 irradiation with neutral density light filters. The steady-state efficiencies were obtained by
3 tracking the maximum power point. All characterizations and measurements were performed
4 in ambient. The single top cells, single bottom cells, and 2-T tandem cells with an active area
5 of 0.105 cm² as defined by the mask were measured. The stability of the encapsulated solar cell
6 was tested in the ambient, by tracking the steady state efficiency of the device for 5 hours under
7 continuous 100 mW cm⁻² AM1.5 G solar irradiation. EQE spectra for single top and bottom
8 cells were performed from 300 to 1150 nm on a QE system (PV Measurements Inc., model
9 IVQE8-C QE system without bias voltage). The EQE spectra of the bottom and top subcells
10 were measured as described in previous reports^{8,40}. A standard silicon wafer cell was used as
11 the reference for the EQE measurement.

12
13 **Data availability.** The data that support the findings of this study are available from the
14 corresponding author upon reasonable request.

16 References

- 18 1 Kojima, A., Teshima, K., Shirai, Y. & Miyasaka, T. Organometal Halide Perovskites
19 as Visible-Light Sensitizers for Photovoltaic Cells. *J. Am. Chem. Soc.* **131**, 6050-6051,
20 (2009).
- 21 2 Shin, S. S. *et al.* Colloidally prepared La-doped BaSnO₃ electrodes for
22 efficient, photostable perovskite solar cells. *Science* **356**, 167-171, (2017).
- 23 3 NREL. <https://www.nrel.gov/pv/assets/images/efficiency-chart.png>.
- 24 4 Malinkiewicz, O. *et al.* Perovskite solar cells employing organic charge-transport
25 layers. *Nat. Photon.* **8**, 128-132, (2014).
- 26 5 McMeekin, D. P. *et al.* A mixed-cation lead mixed-halide perovskite absorber for
27 tandem solar cells. *Science* **351**, 151-155, (2016).
- 28 6 Stoumpos, C. C., Malliakas, C. D. & Kanatzidis, M. G. Semiconducting Tin and Lead
29 Iodide Perovskites with Organic Cations: Phase Transitions, High Mobilities, and
30 Near-Infrared Photoluminescent Properties. *Inorg. Chem.* **52**, 9019-9038, (2013).

- 1 7 Hao, F., Stoumpos, C. C., Chang, R. P. H. & Kanatzidis, M. G. Anomalous Band Gap
2 Behavior in Mixed Sn and Pb Perovskites Enables Broadening of Absorption
3 Spectrum in Solar Cells. *J. Am. Chem. Soc.* **136**, 8094-8099, (2014).
- 4 8 Eperon, G. E. *et al.* Perovskite-perovskite tandem photovoltaics with optimized
5 bandgaps. *Science* **354**, 861-865, (2016).
- 6 9 Anaya, M., Lozano, G., Calvo, M. E. & Míguez, H. ABX₃ Perovskites for Tandem
7 Solar Cells. *Joule* **1**, 769-793, (2017).
- 8 10 Werner, J. *et al.* Efficient Near-Infrared-Transparent Perovskite Solar Cells Enabling
9 Direct Comparison of 4-Terminal and Monolithic Perovskite/Silicon Tandem Cells.
10 *ACS Energy Lett.* **1**, 474-480, (2016).
- 11 11 Fu, F. *et al.* Low-temperature-processed efficient semi-transparent planar perovskite
12 solar cells for bifacial and tandem applications. *Nat. Commun.* **6**, 8932, (2015).
- 13 12 Forgács, D. *et al.* Efficient Monolithic Perovskite/Perovskite Tandem Solar Cells.
14 *Adv. Energy Mater.* **7**, 1602121, (2017).
- 15 13 Rajagopal, A. *et al.* Highly Efficient Perovskite–Perovskite Tandem Solar Cells
16 Reaching 80% of the Theoretical Limit in Photovoltage. *Adv. Mater.* **29**, 1702140,
17 (2017).
- 18 14 Eperon, G. E., Hörantner, M. T. & Snaith, H. J. Metal halide perovskite tandem and
19 multiple-junction photovoltaics. *Nat. Rev. Chem.* **1**, 0095, (2017).
- 20 15 Song, Z. *et al.* A techno-economic analysis of perovskite solar module manufacturing
21 with low-cost materials and techniques. *Energy Environ. Sci.* **10**, 1297-1305, (2017).
- 22 16 Zhao, D. *et al.* Low-bandgap mixed tin–lead iodide perovskite absorbers with long
23 carrier lifetimes for all-perovskite tandem solar cells. *Nat. Energy* **2**, 17018, (2017).
- 24 17 Bu, T. *et al.* A novel quadruple-cation absorber for universal hysteresis elimination for
25 high efficiency and stable perovskite solar cells. *Energy Environ. Sci.* **10**, 2509-2515,
26 (2017).
- 27 18 Huang, J., Yuan, Y., Shao, Y. & Yan, Y. Understanding the physical properties of
28 hybrid perovskites for photovoltaic applications. *Nat. Rev. Mater.* **2**, 17042, (2017).
- 29 19 Tan, H. *et al.* Efficient and stable solution-processed planar perovskite solar cells via
30 contact passivation. *Science* **355**, 722-726, (2017).
- 31 20 Shao, Y., Xiao, Z., Bi, C., Yuan, Y. & Huang, J. Origin and elimination of
32 photocurrent hysteresis by fullerene passivation in CH₃NH₃PbI₃ planar
33 heterojunction solar cells. *Nat. Commun.* **5**, 5784, (2014).
- 34 21 Shao, Y., Yuan, Y. & Huang, J. Correlation of energy disorder and open-circuit
35 voltage in hybrid perovskite solar cells. *Nat. Energy* **1**, 15001, (2016).
- 36 22 Zheng, X. *et al.* Defect passivation in hybrid perovskite solar cells using quaternary
37 ammonium halide anions and cations. *Nat. Energy* **2**, 17102, (2017).

- 1 23 Xiao, Z. *et al.* Solvent Annealing of Perovskite-Induced Crystal Growth for
2 Photovoltaic-Device Efficiency Enhancement. *Adv. Mater.* **26**, 6503-6509, (2014).
- 3 24 Zhao, D. *et al.* High-Efficiency Solution-Processed Planar Perovskite Solar Cells with
4 a Polymer Hole Transport Layer. *Adv. Energy Mater.* **5**, 1401855, (2015).
- 5 25 Wu, Y. *et al.* Perovskite solar cells with 18.21% efficiency and area over 1 cm²
6 fabricated by heterojunction engineering. *Nat. Energy* **1**, 16148, (2016).
- 7 26 Liao, W. *et al.* Fabrication of Efficient Low-Bandgap Perovskite Solar Cells by
8 Combining Formamidinium Tin Iodide with Methylammonium Lead Iodide. *J. Am.*
9 *Chem. Soc.* **138**, 12360-12363, (2016).
- 10 27 Zhao, Y. & Zhu, K. *J. Phys. Chem. C* **118**, 9412, (2014).
- 11 28 Yang, M. *et al.* Perovskite ink with wide processing window for scalable high-
12 efficiency solar cells. *Nat. Energy* **2**, 17038, (2017).
- 13 29 Liao, W. *et al.* Lead-Free Inverted Planar Formamidinium Tin Triiodide Perovskite
14 Solar Cells Achieving Power Conversion Efficiencies up to 6.22%. *Adv. Mater.* **28**,
15 9333-9340, (2016).
- 16 30 Yang, B. *et al.* Enhancing Ion Migration in Grain Boundaries of Hybrid Organic-
17 Inorganic Perovskites by Chlorine. *Adv. Funct. Mater.* **27**, 1700749, (2017).
- 18 31 Starr, D. E. *et al.* Direct observation of an inhomogeneous chlorine distribution in
19 CH₃NH₃PbI_{3-x}Cl_x layers: surface depletion and interface enrichment. *Energy*
20 *Environ. Sci.* **8**, 1609-1615, (2015).
- 21 32 Sadhanala, A. *et al.* Preparation of Single-Phase Films of CH₃NH₃Pb(I_{1-x}Br_x)₃ with
22 Sharp Optical Band Edges. *J. Phys. Chem. Lett.* **5**, 2501-2505, (2014).
- 23 33 De Wolf, S. *et al.* Organometallic Halide Perovskites: Sharp Optical Absorption Edge
24 and Its Relation to Photovoltaic Performance. *J. Phys. Chem. Lett.* **5**, 1035-1039,
25 (2014).
- 26 34 Zhao, B. *et al.* High Open-Circuit Voltages in Tin-Rich Low-Bandgap Perovskite-
27 Based Planar Heterojunction Photovoltaics. *Adv. Mater.* **29**, 1604744, (2016).
- 28 35 Johnson, S. R. & Tiedje, T. Temperature dependence of the Urbach edge in GaAs. *J.*
29 *Appl. Phys.* **78**, 5609-5613, (1995).
- 30 36 Zanatta, A. R. & Chambouleyron, I. Absorption edge, band tails, and disorder of
31 amorphous semiconductors. *Phys. Rev. B* **53**, 3833-3836, (1996).
- 32 37 Burlingame, Q. *et al.* Centimetre-scale electron diffusion in photoactive organic
33 heterostructures. *Nature* **554**, 77, (2018).
- 34 38 Song, Z. *et al.* Perovskite Solar Cell Stability in Humid Air: Partially Reversible Phase
35 Transitions in the PbI₂ - CH₃NH₃I - H₂O System. *Adv. Energy Mater.* **6**, 1600846,
36 (2016).

- 1 39 Cheyns, D., Kim, M., Verreert, B. & Rand, B. P. Accurate spectral response
2 measurements of a complementary absorbing organic tandem cell with fill factor
3 exceeding the subcells. *Appl. Phys. Lett.* **104**, 093302, (2014).
- 4 40 Rajagopal, A. *et al.* Highly Efficient Perovskite–Perovskite Tandem Solar Cells
5 Reaching 80% of the Theoretical Limit in Photovoltage. *Adv. Mater.* **29**, 1702140,
6 (2017).
- 7 41 Yakimov, A. & Forrest, S. R. High photovoltage multiple-heterojunction organic solar
8 cells incorporating interfacial metallic nanoclusters. *Appl. Phys. Lett.* **80**, 1667-1669,
9 (2002).
- 10 42 Che, X., Li, Y., Qu, Y. & Forrest, S. R. High fabrication yield organic tandem
11 photovoltaics combining vacuum- and solution-processed subcells with 15%
12 efficiency. *Nature Energy* **3**, 422-427, (2018).
- 13 43 Hadipour, A. *et al.* Solution-processed organic tandem solar cells. *Adv. Funct. Mater.*
14 **16**, 1897-1903, (2006).
- 15 44 Jie, C., Xia, T. S., A., B. P., Ching - Ping, W. & Ni, Z. Interstitial Occupancy by
16 Extrinsic Alkali Cations in Perovskites and Its Impact on Ion Migration. *Adv. Mater.*,
17 1707350, (2018).
- 18 45 Christians, J. A. *et al.* Tailored interfaces of unencapsulated perovskite solar cells for
19 >1,000 hour operational stability. *Nature Energy* **3**, 68-74, (2018).
- 20 46 Leijtens, T., Prasanna, R., Gold-Parker, A., Toney, M. F. & McGehee, M. D.
21 Mechanism of Tin Oxidation and Stabilization by Lead Substitution in Tin Halide
22 Perovskites. *ACS Energy Lett.* **2**, 2159-2165, (2017).
- 23 47 Han, Y. *et al.* Degradation observations of encapsulated planar CH₃NH₃PbI₃
24 perovskite solar cells at high temperatures and humidity. *J. Mater. Chem. A* **3**, 8139-
25 8147, (2015).
- 26 48 Zhao, J. *et al.* Is Cu a stable electrode material in hybrid perovskite solar cells for a
27 30-year lifetime? *Energy Environ. Sci.* **9**, 3650-3656, (2016).
- 28 49 Lee, H. & Lee, C. Analysis of Ion-Diffusion-Induced Interface Degradation in
29 Inverted Perovskite Solar Cells via Restoration of the Ag Electrode. *Adv. Energy*
30 *Mater.* **8**, 1702197, (2018).
- 31 50 Labban, A. E. *et al.* Improved Efficiency in Inverted Perovskite Solar Cells
32 Employing a Novel Diarylamino-Substituted Molecule as PEDOT:PSS Replacement.
33 *Adv. Energy Mater.* **6**, 1502101, (2016).
- 34 51 Yu, Y. *et al.* Synergistic Effects of Lead Thiocyanate Additive and Solvent Annealing
35 on the Performance of Wide-Bandgap Perovskite Solar Cells. *ACS Energy Lett.* **2**,
36 1177-1182, (2017).
- 37 52 Zhao, D. *et al.* Four-Terminal All-Perovskite Tandem Solar Cells Achieving Power
38 Conversion Efficiencies Exceeding 23%. *ACS Energy Lett.* **3**, 305-306, (2018).

- 1 53 Zhao, D. *et al.* Annealing-free efficient vacuum-deposited planar perovskite solar cells
2 with evaporated fullerenes as electron-selective layers. *Nano Energy* **19**, 88-97,
3 (2016).
- 4 54 Jackson, W. B., Amer, N. M., Boccard, A. C. & Fournier, D. Photothermal deflection
5 spectroscopy and detection. *Appl. Opt.* **20**, 1333-1344, (1981).
- 6 55 Lee, J., Rovira, P. I., An, I. & Collins, R. W. Rotating-compensator multichannel
7 ellipsometry: Applications for real time Stokes vector spectroscopy of thin film
8 growth. *Rev. Sci. Instrum.* **69**, 1800-1810, (1998).
- 9 56 Johs, B. *et al.* in *SPIE's International Symposium on Optical Science, Engineering,*
10 *and Instrumentation.* 30 (SPIE).
11

12 **Acknowledgments**

13 The work at University of Toledo is financially supported by the U.S. Department of Energy
14 (DOE) SunShot Initiative under the Next Generation Photovoltaics 3 program (DE-FOA-
15 0000990) for perovskite tandem device fabrication, Air Force Research Laboratory under Space
16 Vehicles Directorate (FA9453-11-C-0253) for wide-bandgap perovskite synthesis, and the
17 Ohio Research Scholar Program for device modeling and understanding. The work at the
18 National Renewable Energy Laboratory is supported by the U.S. Department of Energy
19 SunShot Initiative under the Next Generation Photovoltaics 3 program (DE-FOA-0000990) and
20 under Contract No. DE-AC36-08-GO28308 with Alliance for Sustainable Energy, LLC, the
21 Manager and Operator of the National Renewable Energy Laboratory.

23 **Author contribution**

24 D.W.Z. and Y.F.Y. conceived the project. D.W.Z. carried out single cell and tandem cell
25 fabrication and characterization. C.C. prepared wide-bandgap perovskite film and devices.
26 C.L.W. fabricated single low-bandgap device fabrication and characterization. Z.N.S
27 participated in tandem cell fabrication and characterization and conducted transient
28 photocurrent measurement and modeling. M.M.J., B.S., and N.J.P. conducted PDS
29 measurements. Y.Y. participated in wide-bandgap perovskite film and device fabrication.

1 C.R.G. and C.W.L. helped with the characterization. D.W.Z., Z.N.S, and Y.F.Y. analyzed the
2 data and wrote the manuscript. K.Z. provided helpful discussions during project and helped
3 with the manuscript preparation. X.Z.Z, G.J.F, and R.G.X. helped with the manuscript
4 preparation. All the authors discussed the results and commented on the manuscript. Y.F.Y.
5 supervised the project.

6

7 **Competing interests**

8 The authors declare no competing financial interests.

9

10 **Additional information**

11 Supplementary information is available for this paper at xxxxxx.

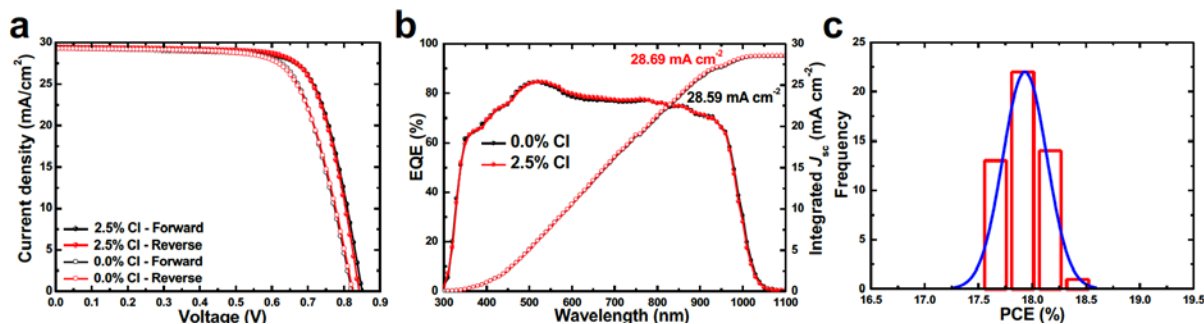
12

13 **Corresponding author**

14 Correspondence and requests for materials should be addressed to D.W.Z. (email:

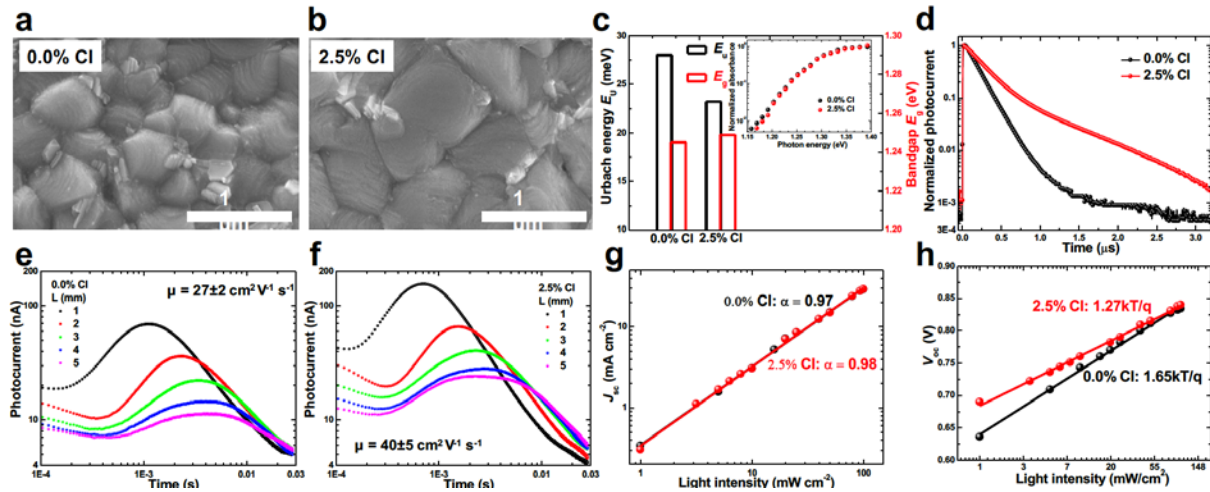
15 dewei_zhao@hotmail.com) and Y.F.Y. (email: yanfa.yan@utoledo.edu).

16



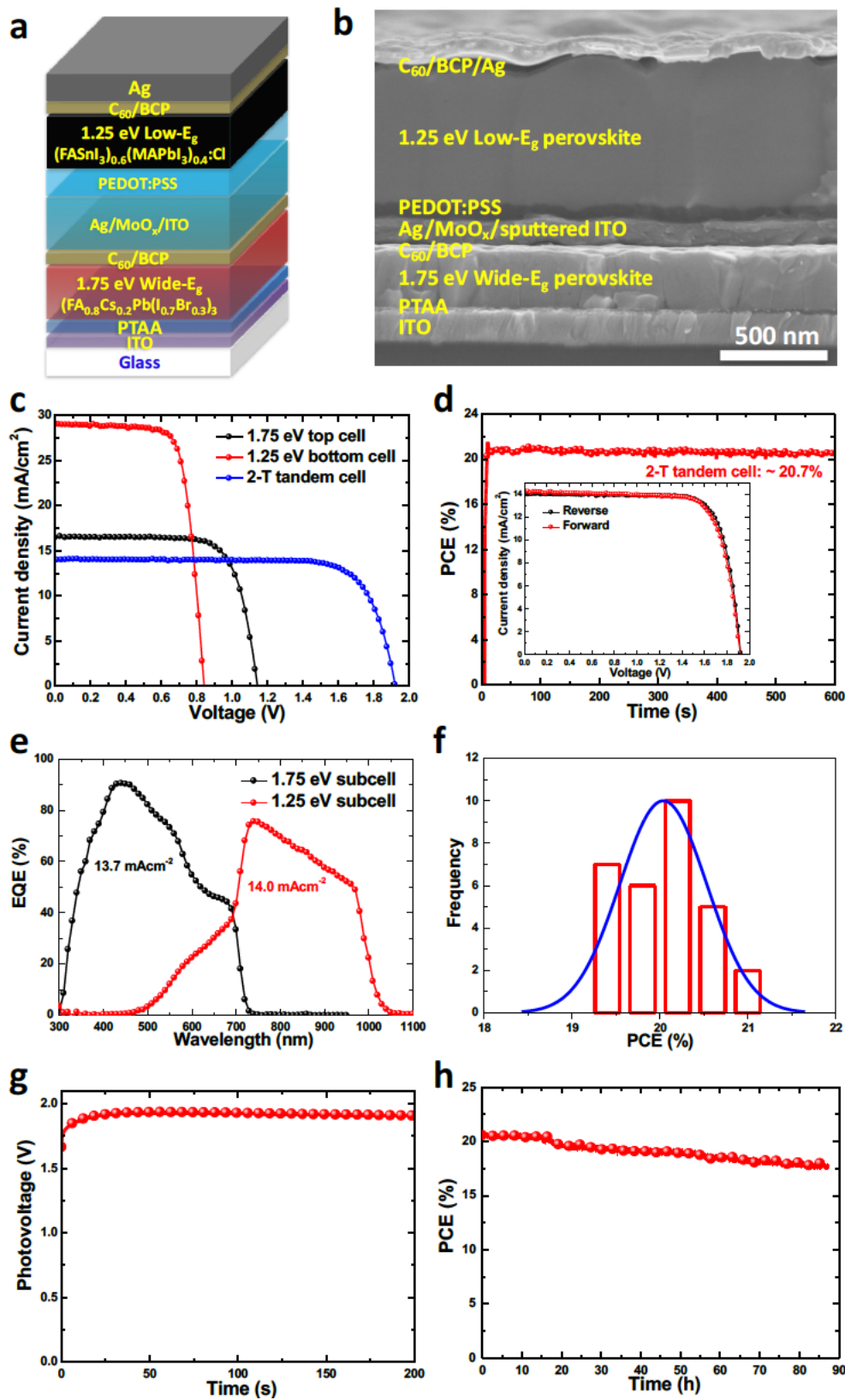
1
2
3
4
5
6
7
8
9
10
11

Figure 1 | Photovoltaic performance of low-E_g solar cells. **a**, The J - V curves under 100 mW/cm² AM1.5 G illumination measured under reverse and forward scans, **b**, EQE spectra and integrated J_{sc} 's of the best-performing low-E_g PVSCs for Sn/Pb-0.0%Cl and for Sn/Pb-2.5%Cl absorbers. The integrated J_{sc} 's over a 100 mW/cm² AM1.5G solar spectrum are 28.59 and 28.69 mA cm⁻² for Sn/Pb-0.0%Cl and for Sn/Pb-2.5%Cl cells, respectively. **c**, Histogram of PCEs measured for 50 cells using Sn/Pb-2.5%Cl absorbers.



1
2
3
4
5
6
7
8
9
10
11
12
13
14
15
16
17
18
19

Figure 2 | Characterization of $(\text{FASnI}_3)_{0.6}(\text{MAPbI}_3)_{0.4}$ perovskite films with 0.0% Cl and 2.5% Cl. **a** and **b**, Top-view SEM images of 0.0% Cl and 2.5% Cl incorporated films, respectively. **c**, Urbach energies and energy bandgaps of films with 0.0% Cl and 2.5% Cl incorporation. Inset shows normalized absorbance of 0.0% Cl and 2.5% Cl incorporated films obtained by photothermal deflection spectroscopy. **d**, Transient photocurrent decay curves of Sn/Pb-0.0%Cl and Sn/Pb-2.5%Cl cells. The variations of room-temperature transient current amplitude and arrival time as a function of L for Sn/Pb-0.0%Cl (**e**) and Sn/Pb-2.5%Cl (**f**) absorbers, where L is the distance between the laser illumination position and the current quench edge of the ITO electrode that is outside of the active area of the device. Sn/Pb-2.5%Cl perovskite film has a hole mobility of $40 \pm 5 \text{ cm}^2 \text{ V}^{-1} \text{ s}^{-1}$ and Sn/Pb-0.0%Cl perovskite film has a hole mobility of $27 \pm 2 \text{ cm}^2 \text{ V}^{-1} \text{ s}^{-1}$. Light intensity-dependence of PVSCs with Sn/Pb-0.0%Cl and Sn/Pb-2.5%Cl absorbers for J_{sc} versus light intensity (**g**) and V_{oc} versus light intensity (**h**), where linear fittings were applied to logarithmic J_{sc} versus logarithmic light intensity (**g**) and to V_{oc} versus logarithmic light intensity (**h**).



2

3 **Figure 3 | Device schematic and performance of 2-T all-perovskite tandem cell. a,**
 4 Schematic of 2-T tandem cell structure used in the study. **b,** Cross-sectional SEM image of an
 5 entire 2-T tandem cell. **c,** J - V curves of single wide- E_g top cell, single low- E_g top cell, and 2-T

1 tandem cell under a 100 mW/cm^2 AM1.5 G illumination measured under reverse scan. **d**,
2 Steady-state efficiencies over time by tracking maximum power output of our champion 2-T
3 tandem cell measured under a 100 mW/cm^2 AM1.5G illumination. Inset shows its J - V
4 characteristics under reverse and forward voltage scans, indicating negligible hysteresis
5 behavior. **e**, EQE spectra of wide- E_g top subcell and low- E_g bottom subcell, operating in the 2-
6 T tandem cell. Their corresponding integrated J_{sc} 's are indicated in the figure. **f**, Histograms of
7 PCEs measured for 30 cells using 1.75 eV top cell and 1.25 bottom cell. **g**, Stabilized
8 photovoltage as a function of continuous illumination time at the open-circuit conditions for a
9 2-T tandem cell. **h**, Steady-state efficiency as a function of continuous illumination time
10 measured by tracking the maximum power output of a 2-T tandem cell.
11
12

1 **Table 1 | Performance of single and 2-T tandem PVSCs.** Summary of device performance
 2 metrics of single wide- E_g (1.75 eV) perovskite top cell, low- E_g (1.25 eV) perovskite bottom
 3 cell, and champion 2-T all-perovskite tandem cell measured under a 100 mW/cm² AM1.5G
 4 illumination under reverse and forward voltage scans.

Cells		V_{oc} (V)	J_{sc} (mA cm⁻²)	FF (%)	PCE (%)
1.75 eV cell	Reverse	1.143	16.4	74.5	14.0
	Forward	1.134	16.5	73.2	13.7
1.25 eV cell	Reverse	0.841	29.0	74.4	18.1
	Forward	0.840	29.0	74.5	18.1
2-Terminal tandem cell	Reverse	1.922	14.0	78.1	21.0
	Forward	1.920	14.1	76.0	20.6

5
6
7